



Crack propagation through sandwich bones due to low-velocity projectile impact

John M. Rickman¹ · James Shackel¹

Received: 31 January 2019 / Accepted: 22 May 2019 / Published online: 8 June 2019
© Springer-Verlag GmbH Germany, part of Springer Nature 2019

Abstract

Projectile impact in sandwich bones typically results in formation of conoidal wounds exhibiting a larger region of damage on the inner cortical plate termed the bevel. To date, a number of hypotheses have been put forward to explain the formation of this wound type. The plug and spall hypothesis suggests that the conoidal morphology is produced by a two-phase mechanism of shear plug formation followed by internal bevel production during projectile exit. In contrast, the cone crack hypothesis suggests that such wounds are produced by cone crack propagation through the three laminae of the sandwich bone, resulting in the formation of bioceramic conoids consisting of all three bone laminae. In order to test these hypotheses, 28 non-human sandwich bones were impacted with 6-mm carbon steel spheres at velocities ranging from 26 to 96 metres per second (m/s). Impacts were filmed utilizing high-speed videography and fracture morphology analysed using micro-computerized tomography (μ -CT). Sequential increase in velocity successfully captured the genesis of conoidal wounds. Low-velocity impact produced circular depressed fractures in the outer cortex exhibiting angulated cortical fracture edges. An increase in velocity resulted in translaminar fracture and production of one intact and three fragmentary bioceramic conoids. At the highest velocities, conoids were fragmented and lost in the ejecta plume, with attached fragments undergoing dynamic movement during and after perforation. Significantly, projectile exit was not required for bevel production. The implications of these findings in wound interpretation are discussed.

Keywords Skeletal trauma · Projectile trauma · Bevelling · Forensic anthropology · Fracture · Trajectory determination

Introduction

The conoidal fracture expressed in sandwich bones subsequent to projectile impact is an intriguing traumatic feature upon which critical diagnostic and trajectory determinations are based [1–4]. Morphologically, this wound type consists of a conoidal wound volume bordered by a fracture edge through all three layers of the sandwich bone, extending from the entry point in the outer cortex and across the intervening trabeculae to the inner cortical lamina [5]. Such conoidal fracture morphology dictates that the region of missing bone in the inner cortical lamina has a larger surface area than that missing from the opposing cortical entry wound. The bony layers

composing this flaring, termed the internal bevel in entry wounds and external bevel in exit wounds [1, 6], are rarely formally defined; however, it is accepted that the conoidal fracture extends in the direction of projectile travel and thus indicates the entry or exit status of the wound [6, 7]. Further diagnostic emphasis has been placed on the symmetry of the bevel, with regions of bevel elongation considered to indicate the trajectory of the projectile through the bone [2, 3, 8], although full correlation between these variables has been disputed [5, 9]. Despite the importance of such determinations in forensic contexts, there is still no consensus in the literature as to the mechanisms underlying formation of this conoidal wound type, and multiple medicolegal cases have now demonstrated that this feature is not unique to projectile impact [10].

In material terms, bone is a bioceramic composite [11] with hierarchical organization [12–14]. At the macroscopic level, the sandwich bones of the neurocranium are constructed of outer and inner layers of cortical bone separated by an intervening trabecular layer of variable thickness, sometimes termed the *diploë* [15]. Fractures through such a sandwich bone may be confined to a single layer (intra-laminar), cross

✉ John M. Rickman
j.m.rickman@cranfield.ac.uk

James Shackel
j.shackel@cranfield.ac.uk

¹ Cranfield Defence and Security, Defence Academy of the United Kingdom, Cranfield University, Shrivenham SN6 8LA, UK

one or more layers (trans-laminar) or pass between layers (inter-laminar, or delamination) [5]. These fractures may be further classified according to mechanism; mode 1 failure indicates a tensile, crack opening mode whilst mode 2 refers to in-plane shear, which occurs in the absence of crack opening [16].

For descriptive purposes, the current paper utilizes nomenclature developed from the micro-computerized tomographic (μ -CT) analysis presented previously by the present authors [5]. In this scheme (Fig. 2), a single conoidal entry wound in a sandwich bone is considered to consist of a cortical entry in the outer cortical layer and a cortical exit in the inner cortical layer, the two encompassing the upper and lower borders of an internal conoidal wound volume. Entry cortical fracture edges form the walls of the cortical entry whilst the cortical exit is bound by the walls of the exit cortical fracture edge. The trabecular fracture margin is formed by the free edges of fractured trabeculae, and peripheral trabeculae are those trabeculae up to 3 mm peripheral to this margin. This entry cortical fracture edge is typically angulated and the crack producing this cortical fracture margin crosses with little to no deviation across the trabeculae and into the inner cortex as a translaminar fracture surface. Such continuous translaminar fracture renders definition of the layers composing the internal bevel an arbitrary process; however, the present paper defines the internal bevel as a conoidal wound volume encompassing the exit cortical fracture edge and trabecular fracture margin.

The plug and spall hypothesis is the most widely cited mechanism for production of this wound type, appearing in multiple standard texts considering the subject of osseous gunshot wounds [e.g. 3, 7, 17]. This hypothesis (see Fig. 1) proposes that conoidal wound formation is a two-phase process involving plug formation in the outer cortex and then bevel production. In the first phase, projectile impact shears a plug or disc of cortical bone from the outer cortical layer [3, 18, 19] (Fig. 1a). This shear plug is then theorized to move ahead of the projectile through the sandwich structure (Fig. 1b), with some interpretations also suggesting that fractured material accumulates ahead of the projectile/plug combination [19]. In the second phase, the internal bevel is believed to be formed by a blow-out process involving fracture or “spall” around the plug during projectile exit (Fig. 1c) [3, 7, 18], with plug-induced shear through the trabeculae posited as a specific mechanism for trabecular failure [4]. Kieser et al. [19] utilized μ -CT to analyse wound cross-sections and proposed that the resultant wound profile due to cortical plug production was funnel shaped, with the neck of the funnel in the external cortex (Fig. 1d). According to the plug and spall hypothesis, the dominant fracture mechanism is considered to be mode 2 (in-plane shear).

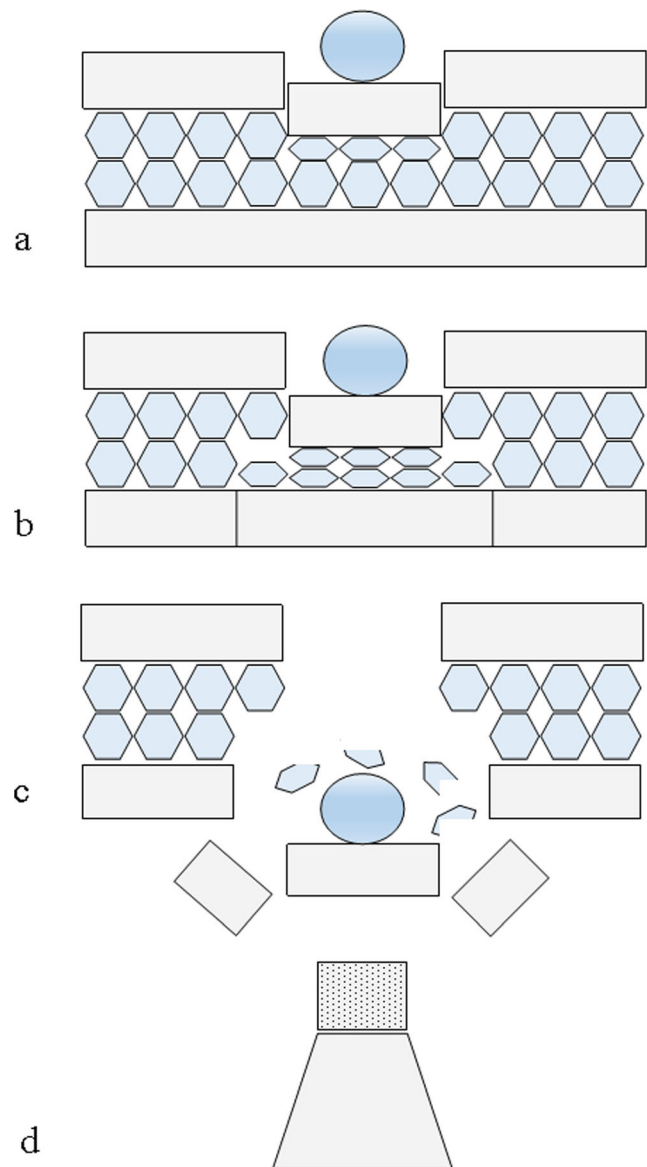


Fig. 1 The plug and spall hypothesis. **a** Projectile impact shears a plug of cortical bone from the outer cortical layer. **b** Projectile and sheared plug move through the trabecular layer, signified by hexagons; note cell collapse and densification due to compressive stresses. **c** Projectile and shear plug blast out the exit to produce the internal bevel. **d** Wound volume profile in section as proposed by Keiser et al (2013); wound is funnel shaped, with vertical neck in the outer cortex (dotted region) and conoidal region through the trabecular layer and internal cortical layer

The plug and spall hypothesis, as described above, involves several key assumptions:

1. Plug production through in-plane shear is independent of projectile tip shape and construction, since conoidal wounds are not restricted to certain projectile designs.
2. The disc of sheared bone does not fragment during transit through the sandwich structure.
3. The projectile must pass through the trabeculae and then exit the bone for the bevel to form

Despite wide usage of this hypothesis, there appears to be no published evidence supporting the role of a cortical plug in wound formation. Shear plugging itself is sensitive to multiple factors including target material characteristics, projectile tip shape, velocity, and angle of impact [20], and thus it will not occur with all impacts in a given material. Recognition of the high-contact stresses developed during impact raises the question as to how a shear plug could participate in perforation without itself being destroyed during the impact event. Analysis of high-speed footage of projectile exit through pig sandwich bones has revealed no evidence for an intact disc of cortical bone exiting ahead of the projectile [5]. Furthermore, cross-sectional analysis has demonstrated that the bevel still forms when it is shielded behind bone fragments retained on the inner cortical plate, effectively ruling out bevel production due to contact with a disc of cortical bone in those regions [5].

In an alternative hypothesis based upon a μ -CT and high-speed video analysis (Fig. 2), Rickman and Shackel [5] proposed that the conoidal wound in sandwich bones is produced by cone crack formation under tension in the outer cortex; this cone crack was then theorized to propagate through the trabecular lamina one cell width at a time before finally entering the inner cortex. According to this scheme, the crack propagates through the tri-laminar sandwich bone as if it were a homogeneous solid, resulting in production of a conoidal structure consisting of all three layers of the sandwich bone, separated from the parent bone by the conoidal fracture, or bevel. This tri-layered plug, or bioceramic conoid, would be identical to the ceramic conoids produced during impact of

non-biogenic ceramics [21] but with the addition of a layer of trabecular bone running between cortical plates. Morphological evidence in support of the cone crack hypothesis and bioceramic conoid formation at higher velocities included angulation of the entry cortical fracture edges, apparent trans-laminar fracture through the sandwich structure and part-counterpart relationships between fragments of inner cortical plate and the internal bevel. Unlike the plug and spall theory, the cone crack hypothesis does not assume that projectile exit is required to produce the bevel. Rather, the bevel is theorized to form at the moment of impact by a cone crack propagating at the speed of sound through the material from outer to inner cortical plates. Unlike the plug and spall theory, the cone crack hypothesis suggests that the fracture driving wound formation is primarily a crack opening, mode 1 (tensile) process.

A significant complication when studying plugs during high-velocity impact arises from the fact that plug fragmentation in brittle materials occurs as little as 10 % beyond the minimum perforation velocity [20]; accordingly, their possible formation above this threshold must be inferred from residual fracture morphology. At present, evidence of intact projectile-induced bioceramic conoids in sandwich bones is limited to a few reports in the archaeological and forensic literature of tri-layered plugs that demonstrate part-counterpart relationships with their parent bone [22–24]. However, whilst these valuable finds indicate that conoidal plugs can be produced during at least some projectile impacts, it is not yet clear if their production underlies the formation of all conoidal wounds.

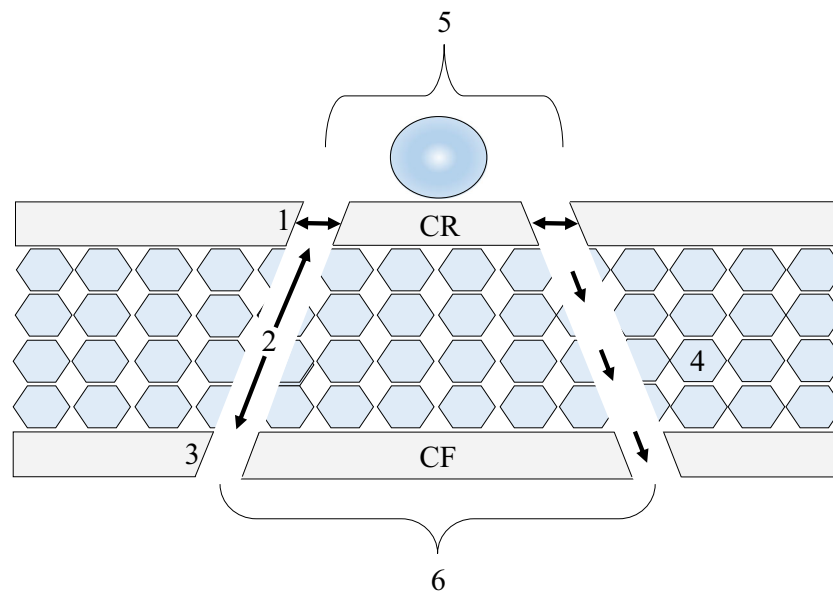


Fig. 2 The cone crack hypothesis and formation of a tri-layered plug or bioceramic conoid; projectile impact elicits cone crack formation under tension in the outer cortical layer (horizontal double headed arrows); crack then propagates under tension through the trabecular cells and through the inner cortical layer (three arrows descending at right); nomenclature for

cross-sectional anatomy presented in [5]; 1, entry cortical fracture edge; 2, trabecular fracture margin; 3, exit cortical fracture edge; 4, peripheral trabeculae; 5, cortical entry; 6, cortical exit; the bevel is here defined as the trabecular fracture margin (2) and exit cortical fracture edge (3); intact bioceramic conoid has a cortical roof (CR) and a cortical floor (CF)

To date, no published accounts of their experimental formation could be identified and, accordingly, there is much to be learned about how these structures form and about their possible wider role in conoidal wound formation in sandwich bones.

An alternative approach to the study of crack propagation from post-perforation fracture morphology is to utilize a series of low-velocity increments in an attempt to capture crack propagation through the depth of the structure. Although the assumption that low- and high-velocity impacts elicit identical fracture behaviours may not always be met due to both strain rate and shock wave effects, this technique was successfully utilized by Kieser et al [25] to capture the formation of butterfly fractures in deer femora, a fracture type typical of higher-velocity impacts in long bone shafts. Significantly, these authors also reported cone crack propagation in the compact bone. Although informative footage of long bone projectile perforation has been captured by high-speed videography [26–28], visualization of fracture processes in sandwich bones is currently limited to high-velocity tangential impacts to synthetic analogues [29] and perpendicular impacts to pig scapulae [5]. To further test the plug and spall and cone crack hypotheses, the present study utilizes a combination of μ -CT and high-speed videography to capture crack propagation processes in non-human sandwich bones subjected to a series of incremental low-velocity impacts between 25 m/s (metres per second) and 100 m/s. Fracture processes are described and their significance in relation to wound diagnosis and interpretation is then discussed.

Methods

Adult domestic pig (*Sus scrofa*) scapulae derived from the food chain were selected as proxies for human bones due to the fact they exhibit bevelled wounds when subjected to ballistic impact. Specimens were prepared according to the methods presented in [5]. In brief, only specimens with a layer of soft tissue in the infraspinous fossa, which was selected due to its larger size, were utilized. The glenoid, neck and spine were removed using a band saw, as was a section of cartilage on the anatomically dorsal surface. A target region of the infraspinous fossa no less than 40 mm from any edge was then selected and marked. During impact, specimens were secured in a specially constructed steel clamp that allowed full adjustment for different specimen sizes (Fig. 3). All specimens were impacted with the ventral region forming the apex, the broader dorsal region forming the base and the infraspinous fossa facing outwards.

Surface-hardened 6-mm carbon steel spherical projectiles (Atlas Ball and Bearings, UK) weighing 0.885 g were selected to prevent yaw or deformation from influencing fracture behaviour. These projectiles were fired from a compressed air-

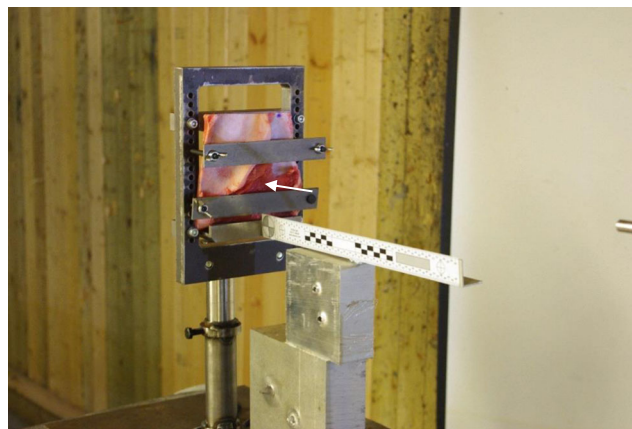


Fig. 3 Machined specimen mounted in adjustable clamping apparatus; target area in the infraspinous fossa indicated by arrow

powered gas gun capable of achieving a velocity range of approximately 25 to 150 m/s. In order to achieve desired incident velocities for the 6-mm spheres, a calibration curve of pressure versus velocity was created in a series of test shots. During the bone impacts, a muzzle-target distance of 60 cm was chosen to prevent discharged air from influencing fracture processes.

Incident (pre-impact) velocity, residual (post-impact) velocity and energy absorption values were determined by placing a Phantom V12 camera to the side of the specimens with a scale in the image. Impact data was then calculated using the Phantom Cine Viewer (Vision Research, Inc.); to allow for variation in velocity measurements, projectile velocity was taken as the mean of three velocity determinations for each specimen. Assuming that energy is not utilized in projectile deformation and that energy lost due to frictional heating is minimal, energy absorption (ΔE) by the bone in joules (J) was then determined using the following formula:

$$\frac{m (v_1^2 - v_2^2)}{2}$$

where m is the mass of the projectile in grams, V_1 is the incident velocity and V_2 the residual velocity in metres per second (m/s). In order to derive a standard deviation for the individual energy absorption values, which were calculated from the mean of three velocities, the error propagation formula presented in Rickman and Shackel [5] was utilized. Inner cortical plate behaviour was captured in all impacts using a Phantom V12 12 camera facing the inner plate and recording at 40,000 frames per second.

To determine velocities associated with internal crack formation, initial tests were conducted with six specimens divided into three pairs with selected target velocities of 30 m/s, 40 m/s and 50 m/s. Actual achieved test velocities were 26 m/s and 29 m/s (group 1), 35 m/s and 37 m/s (group 2) and 47 m/s and 49 m/s (group 3). μ -CT examination revealed that internal

cracking was restricted to the specimen impacted at 47 m/s; accordingly, velocities above 50 m/s were selected for subsequent analysis. In the latter experiments, a more refined inter-shot variation of 1–2 m/s was achieved by noting the velocity of the first shot at each selected velocity; all subsequent shots were then discharged with the same air pressure. Utilizing this method, specimens were impacted between 54 and 55 m/s (group 4), 57–58 m/s (group 5), 74–75 m/s (group 6) and 95–97 m/s (group 7). The number of specimens impacted across these velocities is provided in Table 1. Following Goldsmith [30], penetration was considered to occur if the projectile rebounded and induced surface damage to the specimen (including soft tissue) or if it embedded in the target; perforation occurred if the projectile exited the sandwich bone.

In order to remove the concealing effect of soft tissue when observing fracture, soft tissue was dissected away from the outer and inner cortical layers of six additional specimens. Footage of entry and exit was then obtained by placing the Phantom V12 camera at the rear of each specimen and the Phantom V12 camera at the front; both cameras were then set to record on the same trigger. Although lack of a camera mounted to the side meant that incident velocities could not be determined from imaging of the projectile, the calibration curve allowed velocity estimation to within approximately 1–2 m/s. Inner cortical plate behaviour during projectile rebound was captured using four specimens impacted at approximately 57 m/s. To view the full perforation process at higher

velocity, two final specimens were impacted at approximately 150 m/s. Post-impact analysis revealed that a technical fault in the trigger time of one camera had resulted in a variable delay between front and rear footage, preventing full camera synchronization; however, valuable data on fracture processes was obtained.

Micro-computerized tomography

Specimens were wrapped in cling film, mounted in foam blocks and held securely in place using tape. The impact area of the fleshed specimens was identified and scanned in a Nikon X-Tec XT H 225 scanner at 75 kV, 90 μA and 2.25 magnification, resulting in a voxel size of 89 μm. Scan data was reconstructed using CT Pro 3D; the radius of reconstruction was reduced from 100 to 95–90% in order to remove edge artefacts produced by rotation of the flat plate around the damage area. Reconstructed volumes were analysed in VGStudeo MAX version 2.2 (Volume graphics, Germany). The simple registration function was utilized to orientate specimens across the middle of the screen with the cortical entry facing upwards. Bone surfaces were identified using the surface determination function. Distance and angle-measuring tools were set to recognize and attach to the bone surface using the snap to surface function, allowing precise placement of the tool. The depth of depressed fractures at the impact location was obtained by placing a line across the cortical entry and

Table 1 Summary data for *n* = 22 impact events; *n* = number of specimens; velocities from 26 to 49 m/s were grouped into three pairs of initial test shots with the velocity indicated; *S*, penetration of soft tissue only; *SB*, penetration of soft tissue and bone; *E*, projectile embedded in bone; *EnCF*, entry cortical fracture edge; absence of cracks or cracks that

were too small for accurate measurement in the longitudinal plane resulted in the mean entry cortical fracture edge angle being determined from the sample size indicated in parentheses (groups 4, 5 and 7); angle range indicated in italics

Group	Incident velocity (m/s) (<i>n</i>)	Penetration	Perforation	Ring crack/compressed cortical disc	Angulated entry cortical fracture edge	Tri-layered bioceramic conoid (I, intact; F, fragmentary)	Longitudinal plane; mean apical EnCF angle	Longitudinal plane; mean basal EnCF angle
1	26 (1)	S	–	–	–	–	–	–
	29 (1)	S	–	–	–	–	–	–
2	35 (1)	S	–	–	–	–	–	–
	37 (1)	S	–	–	–	–	–	–
3	47 (1)	SB	–	1	1	0	–	–
	49 (1)	S	–	0	0	0	–	–
4	54–55 (3)	3 SB	–	3	3	0	55.31 (2) <i>49.24–61.37</i>	64.82 (2) <i>52.57–77.07</i>
5	56–58 (6)	4 SB; 1 S	1	4	4	1 I	50.33 (3) <i>36.74–62.70</i>	47.00 <i>36.34–53.37</i>
6	73–75 (3)	–	3	3	3	3 F	45.94 <i>44.17–48.97</i>	39.42 <i>27.28–49.34</i>
7	94–96 (4)	2, E	2	–	4	0	44.44 <i>31.19–57.99</i>	53.05 (3) <i>31.98–70.28</i>
Total	22	16	6	11	15	4		

then dropping a distance-measuring tool from this to the most compressed region of cortex.

Cortical entry shape and bevel symmetry

Cortical entry shape was classed as circular, oval or irregular; entries were further classed as circular-irregular or oval-irregular if there was irregularity in part of their otherwise symmetrical margin. Bevel symmetry was determined using μ -CT scans in 3D view and by descending through the wound to the exit cortical fracture edge (ExCF). Asymmetrical bevels were defined as those presenting a deviation in the ExCF resulting in a more pronounced bevel margin in one or more areas; in symmetrical bevels, the ExCF showed no such deviation.

Results

A total of 28 specimens were impacted and filmed, with side on camera footage available for 22 of these; summary data for these 22 impacts is provided in Table 1. Energy absorption values could not be calculated in the two group one specimens; in one, projectile re-bounce was not captured, whilst in the other the projectile immediately re-bounced off the clamp. Figure 4 shows the relationship between incident velocity, energy absorption and whether impact resulted in re-bounce, penetration or perforation for the remaining 20 specimens. Across these impacts, absorbed energy ranged from 0.48 to 4.08 J. An increase in incident velocity resulted in a steep increase in energy absorption. In specimens retaining soft tissue, a total of 16 impacts resulted in penetration, with 14 of these undergoing rebound. Two impacts at the highest velocities in the series (at 94 m/s and 96 m/s) resulted in embedment. In total, perforation was observed in 6 specimens and was found to initiate at 58 m/s. Greater absorbed kinetic

energy above this threshold resulted in perforation in five of the seven impacts between 73 and 96 m/s.

Measurement data taken from the four specimens impacted between 94 and 96 m/s suggested factors that might have determined whether projectile penetration or perforation occurred (Table 2). Apical and basal total thicknesses, apical and basal trabecular thicknesses and apical cortical thicknesses were greater in the two embedding impacts. This general trend for a thicker outer cortex in the embedding impacts also existed for the basal side of the wound, although there was overlap between the 96 m/s perforation and 96 m/s embedment. Apical and basal thicknesses of the inner cortical layers were also greater in the two embedding impacts. The thickness of the trabecular lamina in relation to whole bone thickness did not appear to influence projectile behaviour, with one perforating impact actually having a proportionally thicker trabecular layer than the two embedding impacts. Projectile embedment was associated with greater energy absorption in both cases.

Table 3 details external wound morphology in the 6 perforated fleshed specimens. The majority of entries were circular ($n = 3$) or circular-irregular ($n = 2$). The single irregular entry occurred at the lowest incident velocity and in a very thin specimen (0.9 mm at its thinnest point). The majority of bevels ($n = 4$) were asymmetrical. Only one of the three circular entries exhibited symmetrical bevelling.

External and internal fracture morphology

Rebound impacts between 26 and 58 m/s resulted in splitting and retraction of the periosteum at the impact site. In all impacts between 26 and 37 m/s, damage was entirely limited to soft tissue. Rebound impacts induced between 47 and 58 m/s resulted in partial or full penetration of the outer cortical plate. Penetration was associated with formation of a cortical entry bordered by a circular, ring-type crack and a compressed disc of cortex located immediately

Fig. 4 Relationship between incident velocity (m/s), energy absorption (J) and projectile behaviour during impact; re-bounce (triangles); perforation (diamonds) and penetration (squares)

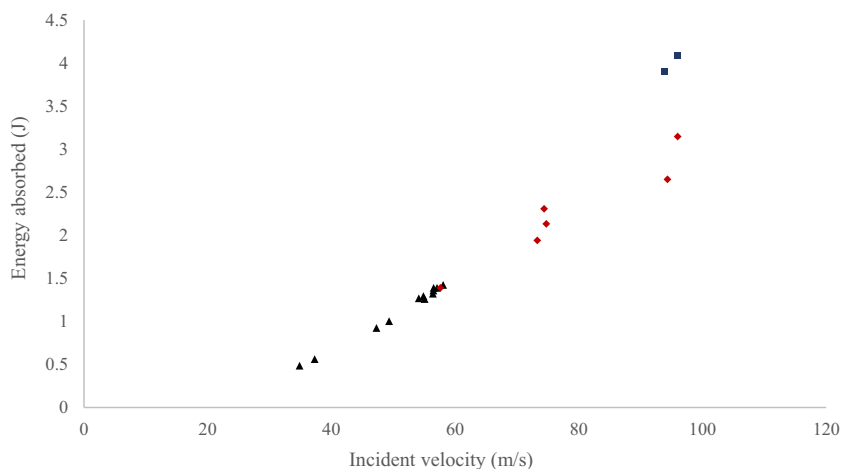


Table 2 Projectile behaviour and energy absorption (J) in relation to total bone thickness, thickness of the outer and inner cortical layers and trabecular thickness; data derived from μ -CT using $\rho-z$ (longitudinal) sections; each thickness measured as close to the wound volume as possible; standard deviation for energy absorbed in parentheses was calculated using the error propagation formula in [5]

Incident velocity (m/s)	Projectile behaviour	Total bone thickness (TB), apical (mm)	Total bone thickness (TB), basal (mm)	Outer cortical thickness, apical (mm)	Outer cortical thickness, basal (mm)	Inner cortical thickness, apical (mm)	Inner cortical thickness, basal (mm)	Trabecular thickness apical (mm)	Trabecular thickness (T), basal (mm)	Trabecular proportion (T/TB), apical	Trabecular proportion (T/TB), basal	Energy absorbed (J)
94	Embedment	5.74	6.20	1.34	0.96	0.85	0.92	3.35	4.06	0.58	0.65	3.90 (0.01)
96	Embedment	5.80	6.34	1.04	0.92	0.99	0.72	3.55	4.55	0.61	0.72	4.08 (0.01)
91	Perforation	4.17	4.05	0.71	0.62	0.62	0.47	2.95	2.82	0.71	0.70	2.65 (0.01)
96	Perforation	1.92	3.09	0.99	0.92	0.51	0.68	0.51	1.48	0.27	0.48	3.15 (0.0002)

Table 3 Cortical entry shape and bevel symmetry in relation to incident velocity for perforated specimens

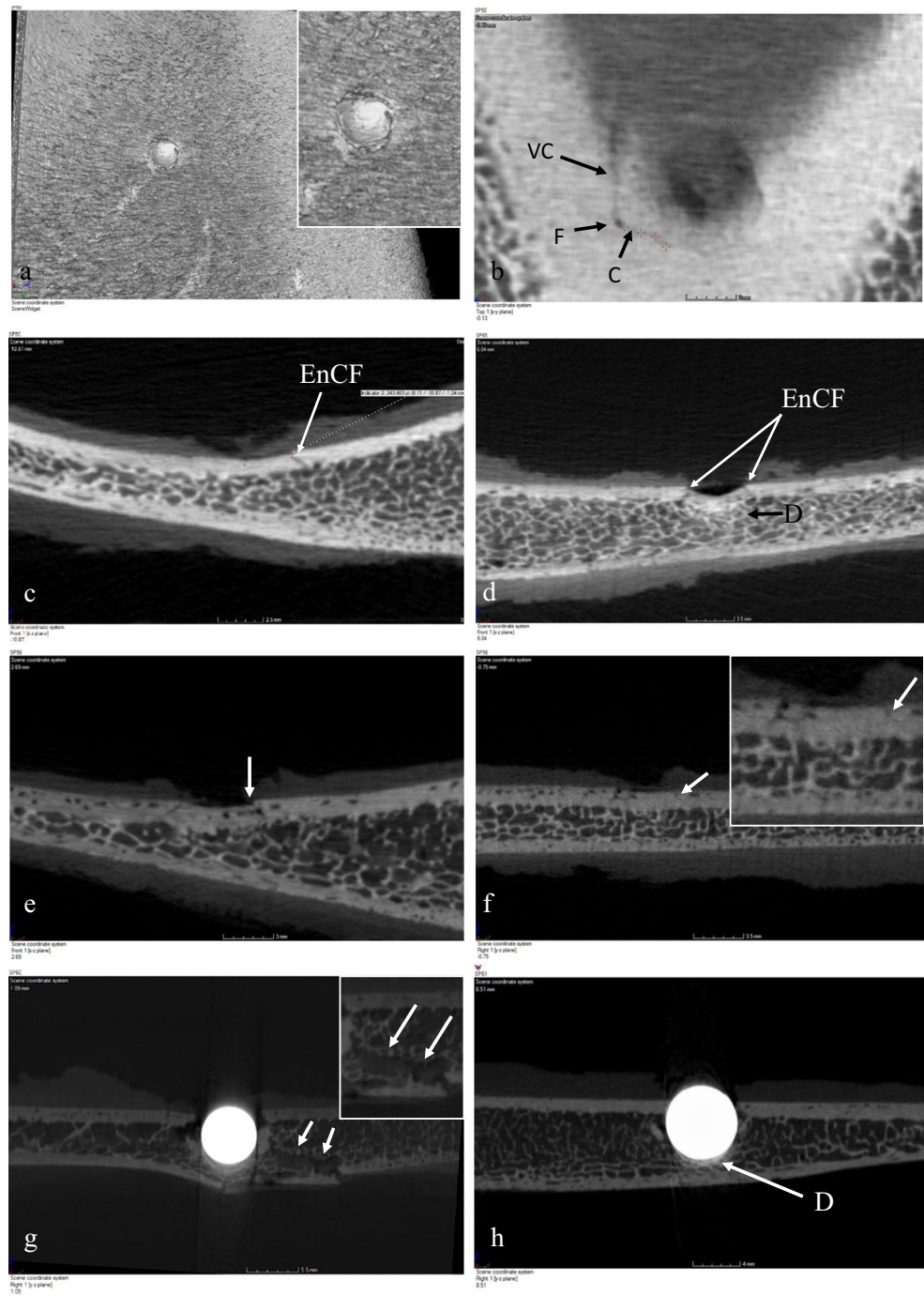
Group	Incident velocity (m/s)	Cortical entry shape	Bevel symmetry
5	58	Irregular	Asymmetrical
6	73	Circular-irregular	Symmetrical
6	74	Circular-irregular	Asymmetrical
6	75	Circular	Asymmetrical
7	91	Circular	Asymmetrical
7	96	Circular	Symmetrical

under the impact location (Fig. 5a). Compressed cortical discs and ring-type cracks were present in the outer cortex of 8 of the 10 rebound impacts between 47 and 58 m/s. The two remaining specimens in this velocity range exhibited no signs of fracture despite one being the highest-velocity impact resulting in rebound at 58 m/s.

The flaws giving rise to the ring-type cracks were below the limit of resolution of the μ -CT in all but one specimen, where a crack emanated from a nutrient foramen in the outer cortical plate before taking a circular course and completing a semi-circular fracture at the impact location (Fig. 5b). In cross-section, specimens exhibited various degrees of compression of the cortical disc, ranging from minimal (Fig. 5c, incident velocity 47 m/s, approximately 0.38-mm compression) to just over a millimetre (Fig. 5d, incident velocity 54 m/s, approximately 1.19-mm compression). Despite being bent from above downwards, plastic deformation occurred without signs of tensile fracture on the inner aspect of the cortical discs (e.g. Fig. 5d). No specimens exhibited any sign of the disc being displaced downwards as an intact shear plug into the trabeculae. Trabecular cells underneath one heavily compressed cortical disc had undergone a degree of cell collapse, resulting in some densification of the cellular solid (Fig. 5d).

Cross-sectional analysis of the compressed cortical discs revealed that fracture of the sandwich bone was restricted to the outer cortical layer in all but one specimen (discussed below). In cross-section, the cortical walls of the circular cracks were angulated with respect to the cortical surface in cone crack fashion, and presented a relatively straight (e.g. Fig. 5e) or gently curving edge (e.g. Fig. 5f). These angulated fracture surfaces were morphologically identical to those seen in fully formed conoidal wounds and may thus be termed entry cortical fracture edges (Fig. 5c–e). Mean apical and basal angles of these fracture edges together with ranges are presented in Table 1. Mean apical and basal angles showed a general decrease with velocity, although the highest velocity impacts in group 7 resulted in higher basal angles than those in group 6. There was great variation in the angles both within and across groups and around the perimeter of a single cortical entry. For example, whilst the apical angle in one specimen impacted at 57 m/s was 62.70°, the angle on the left side of the

Fig. 5 **a** Example of compressed disc of cortical bone at the impact site. **b** Ring crack (C) originating from nutrient foramen (F) with vascular canal (VC) running vertically. **c** Transverse section of ring crack in **b** showing incipient conoidal wound formation with the presence of an angulated entry cortical fracture edge (EnCF); note minimal compression of the cortex under the impact point. **d** Example of cortical disc showing more extensive compression with some densification (D) of the trabecular cells; note bilateral angulation of the EnCF and crack opening adjacent to the compressed disc. **e** Downward movement of the lateral portion of a compressed cortical disc in relation to the EnCF, indicating a mode 2 (in-plane shear) failure component. **f** Example of mode 1 tensile failure without evidence of in-plane shear. **g** Cross-section of projectile embedment with projectile in situ; wound exhibits bilateral angulation of the EnCF with the cortical disc having fractured in the mid-line and displaced laterally; note formation of a conoidal wound volume despite lack of projectile exit, tensile fracture of inner cortical plate and evidence of crack hopping one cell edge to another (white arrows). **h** Cross-section of second projectile embedment showing bilateral angulation of the EnCF, midline fracture of the cortical disc and densification (D) of the trabecular cells



same entry was 45.59° . Angulation of the entry cortical fracture edge was evident in a perforated specimen where the impact site consisted entirely of cortical bone and was only 0.9 mm thick at its thinnest point.

When internal cracking was restricted to the outer cortex, the angulated cracks were open and their formation must therefore have involved a tensile (mode 1) cracking component (Fig. 5c–f). An additional in-plane shear (mode 2) component to failure of the cortical discs was indicated in some specimens by a slight downward displacement of their lateral

fracture surfaces with respect to the entry cortical fracture edge (Fig. 5e, arrow). In one specimen, an angulated crack without associated in-plane shear was observed (Fig. 5f, arrow), suggesting that shear, if it occurs, must follow initial crack opening under tension. Fracture morphology in the outer cortices was thus suggestive of mode 1 or mixed mode 1–2 cracking processes if shear was operative during the impact event.

Two impacts resulted in projectile embedment in the sandwich bone. Although these specimens represented difficult

samples for μ -CT scanning with the projectiles left in situ, scans without removing the spheres to preserve fracture integrity captured details of the penetration process. In section, angulated entry cortical fracture edges were observed in both impacts (Fig. 5g). Neither specimen exhibited an intact cortical shear plug beneath the projectile. Instead, the cortical disc in both cases had been fractured and displaced laterally by the projectile with the fragments so formed remaining in close proximity to the outer cortical layer from which they were derived. Trabecular cell collapse and associated densification of the cellular solid occurred in both impacts but was particularly prominent in the 91 m/s embedment (Fig. 5h, labelled D). Tensile failure of the inner cortical plate was observable in the 96 m/s impact as a vertically orientated crack approximately in-line with the centre of the embedded sphere (Fig. 5g). The latter specimen exhibited a clear internal conoidal morphology despite lack of projectile exit. Bisected trabecular cells consistent with a tensile fracture crossing from one cell edge to another were present on the right of the conoidal volume (Fig. 5g, arrows). The large separation of the lower right portion of the conoidal volume from the parent bone appears to have occurred as the projectile that compressed the densified trabecular bone downwards (Fig. 5g).

Four impacts, at 57 m/s, 73 m/s, 74 m/s and 75 m/s, respectively, resulted in the formation of tri-layered bioceramic conoids (Fig. 6a–h). At 57 m/s, rebound impact left a structurally intact conoidal volume; fragmentation in the three higher velocity perforating impacts resulted in the retention of fragmentary components only. In all cases, the cortical disc derived from the outer cortex was still present in either intact or partially intact form and clearly formed the roof of the conoid. In the rebound impact, this conoidal roof had been compressed downwards without tilting into the trabecular layer, where it contrasted starkly with the spongy bone around it (Fig. 6a). The conoid remained partially attached at one edge to the inner cortical layer, but translaminar fracture had otherwise separated it from the parent bone. Angulated cone fracture propagation without deviation through the sandwich layers was apparent and resulted in a distinct part-counterpart relationship between conoid and conoidal wound (Fig. 6a–c). In section, the outer cortical layer of this conoid was compressed by approximately 1.05 mm and in one part, a delamination in the outer cortical layer was visible (Fig. 6c). In this region, the upper border of the entry cortical fracture edge exhibited little to no angulation and the conoidal crack flared approximately mid-depth in the trabecular layer (Fig. 6c, arrow). The relationships between the fracture morphology of this specimen and a typical conoidal perforating wound are illustrated in more detail in Fig. 6b. Despite formation due to rebound impact, this specimen had a cortical entry (CE) and cortical exit (CEx) and a fully formed internal bevel (IB). The inner cortical plate in this specimen had failed in tension, resulting in the production of radial fractures emanating from a central point

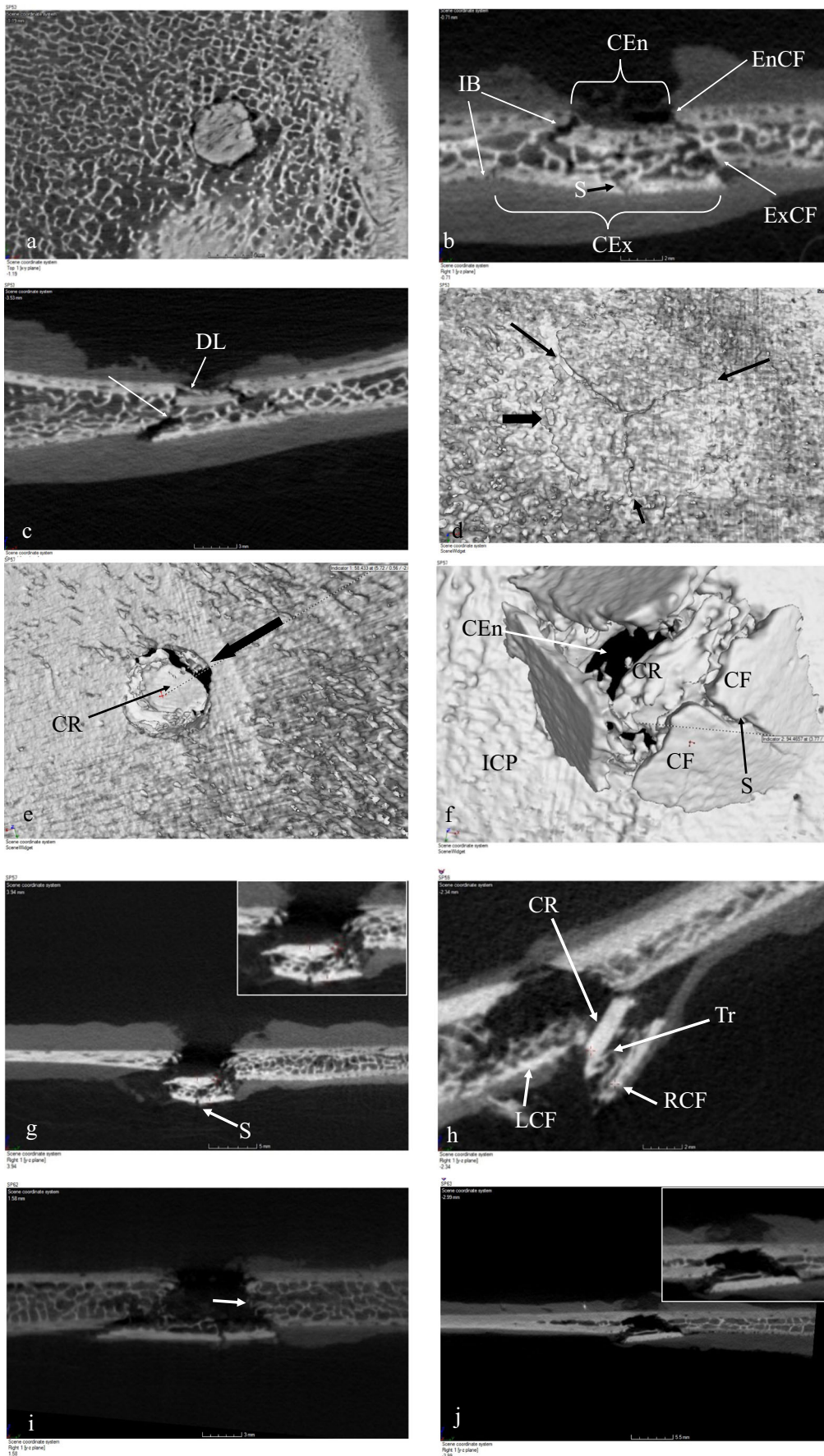
in a stellate pattern (Fig. 6d, thin arrows). These radial fractures arrested at the exit cortical fracture edge, which must therefore have formed first (Fig. 6d, thick arrow). Stellate fracture was detectable in cross-section as an angulated crack in the inner cortical plate (Fig. 6b, labelled S).

In both the 73 m/s and 75 m/s impacts, the fragmentary conoidal volume was tilted and compressed below the inner cortical layer (Fig. 6e–h). The conoidal structure exhibited better preservation in the 75 m/s impact (Fig. 6e–g). Viewed from above, the cortical roof of the conoid was visible through the cortical entry wound (Fig. 6e). The conoid fragments remained attached to the inner cortex on one side (Fig. 6f) and exhibited a tensile fracture that bisected it into two halves. Adjustment of the cross-sectional plane so that it was perpendicular to the displaced three-layered structure confirmed its status as a partial conoid with stellate fracture (Fig. 6g). In the 73 m/s and 74 m/s impacts, the cortical disc forming the roof of the fragmentary conoid was again visible through the cortical entry wound, with the most intact morphology resulting from the 73 m/s impact (Fig. 6h, CR). The presence of a fragmentary conoid in the latter is demonstrated well in cross-section, where both upper and lower cortical components of the structure are readily apparent (Fig. 6h). A single trabecular connection between cortical layers in both the 73 m/s and 74 m/s specimens confirmed that the structures consisted of an entire tri-layered segment of sandwich bone (see Fig. 6h, Tr).

Two higher velocity impacts at 91 m/s and 96 m/s resulted in perforation without retention of any tri-layered fragments. In these specimens, inner cortical plate fragments exhibited part-counterpart relationships with the exit cortical fracture edge and retained some attached trabeculae (Fig. 6i, j). These fragments were therefore identical to the lower portion of the intact bioceramic conoid illustrated in Fig. 6a–c, with their upper parts having been fragmented and ejected. In the 91 m/s impact, some parts of the section through the conoidal wound presented a cleanly fractured edge on one side but exhibited protrusion of the trabeculae into the conoidal wound volume on the other due to alteration in the path of translaminar fracture (Fig. 6i).

High-speed footage of the outer cortical plate

Front on footage of impact at approximately 57 m/s was obtained for four dissected specimens. In this series, rebound occurred in three cases and embedment in the fourth. In all four specimens, impact resulted in a deformation pulse causing vibration at the free specimen edges. In two of the rebound impacts and the embedment, projectile impact resulted in a pulse of elastic deformation in the cortex immediately around the impact point, with rebound occurring during the recoil phase of cortical



◀ **Fig. 6** Bioceramic conoid morphology. **a–d** Intact conoid produced by a 57 m/s impact. **a** Cortical roof of conoid compressed into the trabecular layer. **b** Longitudinal section of conoid showing relationships with typical perforating conoidal projectile wound; CEn, cortical entry; CEx, cortical exit; EnCF, entry cortical fracture edge; ExCF, exit cortical fracture edge; IB, internal bevel; S, stellate fracture. **c** Transverse section showing delamination (DL) of upper cortical layer and flaring of the conoidal crack within the trabeculae (arrow). **d** Inner cortical plate showing exit cortical fracture edge (large black arrow) and radial fractures of stellate fracture pattern (small black arrows). **e–g** Fragmented conoid produced by a 75 m/s impact. **e** View through cortical entry showing depressed cortical roof of conoid and entry cortical fracture edge (arrow). **f** Conoid fragment viewed from inner cortical plate; CR, cortical roof; CF, cortical floor; S, stellate fracture; CEn, cortical entry; ICP, inner cortical plate. **g** Cross-section perpendicular to the conoid fragment visible in **f**. **h** Fragmented conoid produced by 73 m/s impact; CR, cortical roof; Tr, trabecular connection between cortical roof and cortical floor of fragmentary conoid; LCF, left cortical floor and RCF, right cortical floor corresponding to fragments visible in Fig. 8j–l; recoil resulted in the cortical roof (CR) being in line with the left cortical floor (LCF). **i, j**, structures consistent with being the inner cortical vestiges of bioceramic conoids formed by 91 m/s (**i**) and 96 m/s impacts (**j**)

deformation. Estimated rebound times at approximately 58 m/s, taken as the time difference between the frames capturing initial contact and retrograde movement, were 227.23 μ s, 227.24 μ s and 136.34 μ s, respectively. During rebound impacts, projectiles partially penetrated the outer cortex (Fig. 7b), with the compressed cortical discs so formed visible as a whitened region of cortex (Fig. 7c). μ -CT analysis of the specimen illustrated in Fig. 7a–c revealed a vertically orientated fracture in the cortical disc just adjacent to the mid-line (Fig. 7d). Cross-sectional fracture morphology revealed bilateral angulation of the entry cortical fracture edges (Fig. 7e, f), identical in form to that observed in impacted fleshed specimens; densification of the trabeculae was also apparent (Fig. 7f, labelled D). In the penetrated specimen, the projectile fractured the outer cortical layer before moving in a retrograde direction and embedding at a depth of approximately half its diameter in the sandwich bone.

Impact at approximately 150 m/s in two defleshed specimens resulted in full perforation, with a deformation pulse visible at the specimen edges in only one of these. Unlike the 58 m/s impacts, the cortex around the impact site showed no visible signs of elastic deformation. Cortical behaviour under the projectile was captured in one specimen, where a semi-circular section of fractured cortex was visible to the right of the projectile (Fig. 7g). Rather than descending with the projectile through the sandwich structure as a shear plug, this fragment folded downwards as the projectile completed perforation (Fig. 7h). Such behaviour was consistent with this fragment being part of the originally circular cortical roof of a bioceramic conoid, identical in morphology to the fractured discs resulting from both embedding (Fig. 5g, h)

and rebound impact (Fig. 7d–f). Fracture and ejection of the cortical roof left an approximately circular cortical entry (Fig. 7i).

High-speed footage of the inner cortical plate

There was no evidence of an intact shear plug arising from the outer cortical layer in any of the impact events. In contrast, observation of the inner cortical plate revealed a common fracture process between impacts that resulted in intact or fragmentary conoid production and higher velocity impacts that did not. During formation of an intact bioceramic conoid (illustrated in Fig. 8a–c), the tri-layered structure elevated with respect to the inner cortical plate, and the conoid floor simultaneously underwent stellate fracture due to high tensile stresses there (Fig. 8b). As impact proceeded, the conoid then underwent recoil in relation to the exit cortical fracture edge (Fig. 8c). The time taken to reach maximal elevation, measured from the frame prior to damage initiation, was 175 μ s; the total time taken to reach maximum recoil was 600 μ s.

Perforating impact resulting in partial fragmentation of a bioceramic conoid is illustrated in Fig. 8d–f. Impact again resulted in elevation of the conoid floor and stellate fracture (Fig. 8e, arrow). Subsequently, the inner cortical plate fragments formed by stellate fracture then went through a process of elevation and eversion, resulting in their trabecular surfaces facing outwards (Fig. 8f), with some then being ejected. Projectile exit occurred through the aperture created by the inner cortical plate fragments before full eversion. The sequence of elevation, stellate fracture, fragment eversion and ejection occurred in the absence of residual tri-layered fragment morphology at 91 m/s and 96 m/s (Fig. 6i, j), and was also seen in dissected specimens impacted at approximately 150 m/s where fragments were ejected. A sequence of images of capturing the exit process is provided for a defleshed specimen impacted at approximately 150 m/s in Fig. 8g–i.

Retained inner cortical plate fragments underwent considerable dynamic movement which in one case resulted in unusual fragment positions after impact (Fig. 8j–l). In this specimen, also illustrated in cross-section in Fig. 6h, two large conoid fragments were produced to the left and right of the cortical exit, with the right fragment retaining the tri-layered morphology. During impact, the conoid elevated and underwent stellate fracture (Fig. 8j, arrow). Although soft tissue partially obscures the bone in the high-speed footage (Fig. 8k), a feature consistent with the left fragment (black arrow) could be seen elevating adjacent to the right tri-layered fragment (white arrow). Subsequent to projectile exit, fragment recoil resulted in the right fragment covering the left (Fig. 8l). In cross-section, this process resulted in the outer cortex of the tri-layered fragment being level with the inner cortex of the left fragment (Fig. 6h).

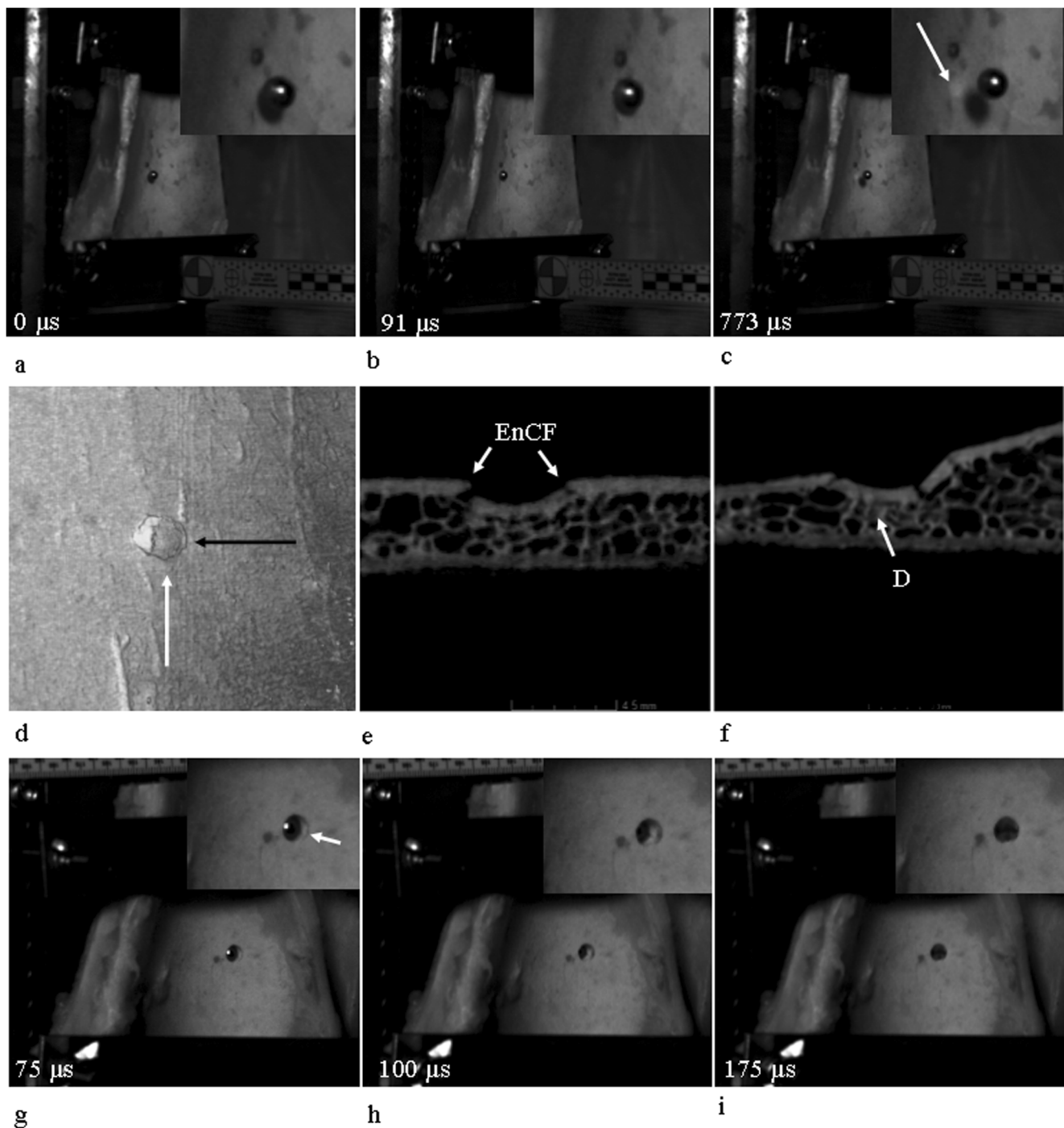


Fig. 7 Rebound and perforating impacts to defleshed outer cortical plates. **a–c** Rebound impact resulting from impact at approximately 57 m/s. **a** Pre-impact. **b** Maximum projectile penetration. **c** Rebound revealing compressed cortical disc (arrow). **d–e** μ CT images of specimen in **a–c**. **d** Three-dimensional view of compressed cortical disc revealing vertical fracture. **e** Section of impact area at approximately mid-cortical entry (direction of section indicated by black arrow in **d**); note angulated entry cortical fractures edges (EnCF) and compression of cortical disc. **f** Section through region of vertical fracture within the

cortical disc (direction of section indicated by white arrow in **d**); note densification of trabeculae (D). **g–i** Perforating impact at approximately 150 m/s, indicated times are from the pre-impact frame (not shown). **g** Projectile has perforated the outer cortical plate, which has fractured and displaced downwards (arrow in enlargement). **h** Projectile has completed exit of the outer cortical plate, revealing fractured and displaced cortical disc still in the process of fragmentation and ejection. **i** Final morphology of cortical entry

Discussion

Projectile perforation is a complex event and the exact mechanisms involved depend upon multiple factors such as target material properties, projectile design and incident velocity [20]. Failure modes can also compete during penetration, with the ultimate mechanism determined by material and projectile characteristics [31]. The complex hierarchical organization of bone also dictates that failure can occur at multiple length scales, introducing a complexity to failure processes that is not typical of synthetic composites [32]. In order to test the plug and spall and cone crack hypotheses, the present study therefore utilized a simplified experimental model consisting of non-human sandwich bones impacted with spherical projectiles. Low-velocity impacts induced using this system successfully captured the genesis of conoidal wounds, at least with the projectile-target combination utilized. Impacts between 26 and 96 m/s resulted in rebound, penetration and perforation, with projectile embedment apparently associated with greater bone thicknesses. Multiple aspects of fracture morphology induced by this range of projectile behaviours did not substantiate the contention that a cortical shear plug participates in perforation and instead were consistent with a tensile, cone cracking process resulting in production of tri-layered bioceramic conoids.

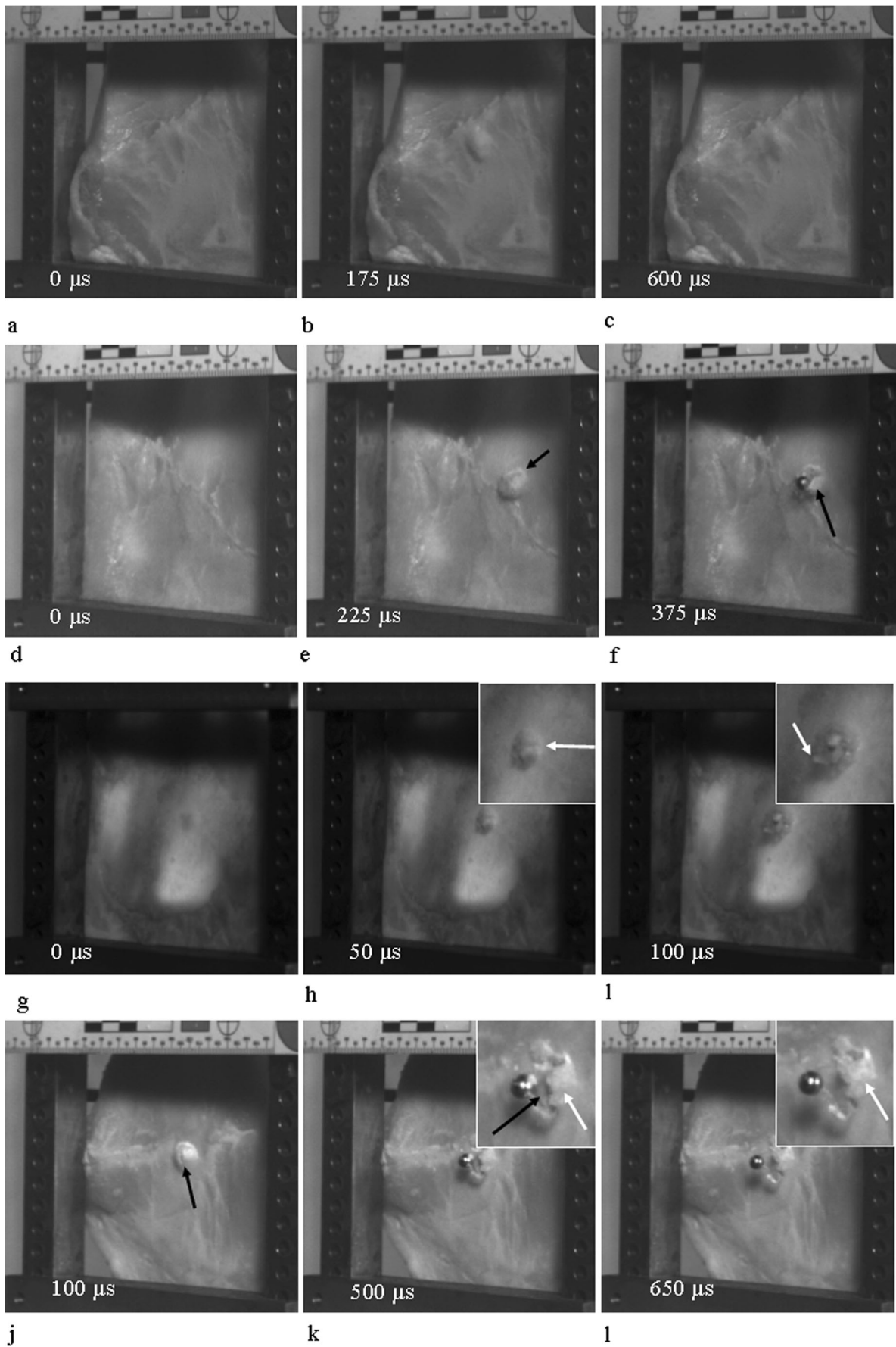
The initial phase of wound formation in rebound impacts below 58 m/s was the production of permanently compressed discs of cortical bone in the outer cortex identical in form to those described in the compact bone of deer femora subjected to sub-100 m/s impact [25]. Although seemingly consistent with shear plug formation when present in sandwich bones, cross-sectional fracture morphology revealed no evidence of these discs being driven through the remaining two sandwich layers, as predicted by the plug and spall hypothesis [4, 7, 18, 19]. In two embedding impacts and high-speed footage of one perforation, the cortical disc underwent fracture in the approximate mid-line and then underwent downward displacement during projectile passage. In four specimens, the cortical disc clearly formed the roof of a bioceramic conoid that displaced downwards as a unit consisting of all three sandwich layers. Significantly, the intact bioceramic conoid induced at 57 m/s shared multiple features with the plugs described in human material by Murphy et al. [22], Murphy et al. [23] and Bird and Fleishman 2015 [24]. Shared structural features included stellate fracture of the inner cortical plate, compression of the outer cortical plate, minimal to no trabecular compression and part-counterpart relationship with the internal bevel in the parent bone. Such morphological correspondence is highly indicative of common fracture processes in human and pig sandwich bones subjected to projectile impact.

A central component of the plug and spall hypothesis is that perforation of the outer cortical layer and bevel formation are separate events, with bevel formation suggested to occur

during projectile exit [e.g. 3, 7, 18, 33, 34]. However, the present study confirms that bevel formation occurs in the absence of projectile exit; indeed, a fully formed conoidal wound was produced by a rebound impact. Numerous lines of evidence now converge to support the hypothesis that production of tri-layered bioceramic conoids is central to conoidal wound formation regardless of incident velocity. In addition to morphological correspondence between experimentally and non-experimentally produced bioceramic conoids, cross-sectional fracture morphology induced by impacts below 100 m/s is identical to that described for impacts between 150 and 897 m/s [5].

The fragmentary nature of three of the conoids formed in the current experiment, coupled with identical deformation and fracture behaviour in perforated specimens lacking conoids, strongly suggests that their absence subsequent to higher velocity impacts is not due to lack of formation but to their complete comminution and ejection, as predicted by the cone crack hypothesis [5]. Incident velocity apparently need not be great to fragment the conoidal volume, with comminution occurring between 73 and 75 m/s. Comminution appears to initiate with midline fracture and downward displacement of the conoidal roof. Subsequently, trabecular cells undergo the process of cell collapse resulting in densification of the trabecular layer. Finally, projectile exit elevates the inner cortical plate fragments and the majority of the conoidal volume is then ejected. Interestingly, the formation of intact conoids highlights a notable difference between biological and synthetic sandwich structures; whilst outer and inner laminae are perforated separately in the latter [35], intact conoid formation does not involve perforation of either layer.

Previous case reports have described conoidal wounds induced by low-velocity impact that are macroscopically identical to those induced at high velocity [36–38], raising a significant diagnostic challenge. The current study indicates that increasing velocity imparts a sequence to conoid behaviour that may assist in such diagnoses. Production of intact conoids was rare, with total fragmentation of the conoidal structure being the norm above 90 m/s. Conoid vestiges produced by impacts in the 73–75 m/s range consisted of variably comminuted outer and inner cortical layers with retained trabecular connections. As velocity increased, conoid collapse from above downwards resulted in loss of the tri-layered morphology, leaving retained inner cortical plate fragments with attached trabeculae as the only vestige of their formation. This morphological data supports the contention of Bird and Fleishman [24] that the retention of intact conoids (termed “plugs” in their article) is consistent with a relatively low-velocity impact event; however, it extends the diagnostic value of these features down to the fragment level. Accordingly, in cases where attached fragments or bony ejecta are retained, it may prove beneficial to search for the vestiges of a tri-layered morphology.



◀ **Fig. 8** High-speed footage of conoid behaviour viewed from inner cortical plate; all times from frame prior to visible damage. **a–c** Damage sequence capturing intact bioceramic conoid behaviour during 57 m/s re-bound impact. **a** Pre-impact. **b** Maximum conoid elevation. **c** Final damage pattern resulting from recoil of conoid. **d–f** 75 m/s perforation that resulted in partial conoid fragmentation. **d** Pre-impact. **e** Early elevation of conoid floor with stellate fracture (arrow) forming inner cortical plate fragments. **f** Eversion of inner cortical plate fragments (arrow). **g–i** Perforation sequence in dissected specimen, approximately 150 m/s. **g** Pre-impact. **h** Elevation and stellate fracture (arrow). **i** Inner cortical plate fragment elevation and eversion (arrow). **j–l** Dynamic movement of conoid fragments during a 73 m/s impact. **j** Stellate fracture of conoid floor (arrow) with central aperture between inner cortical plate fragments. **k** Enlargement shows left cortical floor fragment (black arrow) adjacent to right cortical floor fragment (white arrow). **l** Enlargement shows right fragment has recoiled over left fragment resulting in sectional view visible in Fig. 6h.

Numerous features of fracture morphology were consistent with a cone cracking failure mode. The first stage in cone crack formation during indentation or impact of brittle materials is the initiation of a surface crack from flaws at or slightly outside the contact radius of the projectile in the region of highest tensile stress; this crack then curves around in a circle to produce a ring crack [39–41]. Whilst the origin of the circular crack in the outer cortex was not captured in all specimens, in one, a fracture appeared to originate from a nutrient foramen located in the outer cortex before following a circular path delineating the indented cortical disc. Although a larger sample capturing the origin of such cracks is required to draw definitive conclusions, fracture morphology in this case was inconsistent with a shear failure mode and instead suggested the cortical disc was formed as a result of ring cracking. During cone crack formation, increasing contact pressure from the projectile results in the ring crack flaring to form a cone within the tensile stress field [41]. Similarly, in the present series, all fractured specimens exhibited crack angulation, initiating either in the outer cortical layer, the trabecular layer or both through different parts of the cross-section. Significantly, these angulated cracks were open and in close approximation suggesting the predominance of a tensile, crack opening failure mode. An additional tensile contribution to wound formation appears to arise when the projectile compresses the conoidal volume downwards relative to the trabecular fracture margin, a process that enhances separation of the conoid from the parent bone.

The establishment of projectile trajectory is often a critical aspect of medicolegal investigations [42], with the results of such analyses potentially influencing the outcome of criminal trials [2]. In this regard, the findings presented herein have considerable significance for our understanding of the factors underlying bevel morphology and thus the information that can be gathered from it. At present, prevailing theory indicates that regions of asymmetrical bevelling reflect the trajectory of the projectile [2, 8]. However, work addressing this proposed relationship with human skeletal material reported a poor

correlation between these variables [9]. Bevel asymmetry was also found to be more common than bevel symmetry in experimentally induced perpendicular projectile wounds in pig sandwich bones [5]. The current analysis suggests this trend extends below 100 m/s, with 4/6 perforating wounds between 58 and 96 m/s classified as having an asymmetrical bevel despite resulting from perpendicular impact.

Whilst projectile trajectory in all likelihood does play a part in determining bevel symmetry, the finding that bevel formation occurs in the absence of perforation indicates it is but one of a number of interacting factors underlying bevel shape. The production of bioceramic conoids in the present study confirms that a principle determinant of bevel symmetry must be the path of the translamellar fracture through the sandwich bone subsequent to its origin in the outer cortex. This path will be influenced by material factors such as Poisson's ratio, which is a key determinant of cone crack angle [43], the orientation of the trabecular struts in relation to the advancing crack tip [5] and the presence and distribution of cortical features altering crack direction, such as the cement sheaths of secondary osteons [32]. Loading rate may also play a part in fracture path, with cracks at lower loading rates tending to follow tortuous routes through regions of least resistance and cracks at high loading rates showing no such preference [44–46]. Further quantitative analyses of bevel symmetry and the potential influence of impact angle on this variable are required to quantify the accuracy of bevel shape in trajectory determinations.

The position of retained bone fragments is another indicator that has been utilized to establish trajectory, based on the assumption that their orientation results from direct interaction with the projectile [47]. However, unusual fragment positions can also enhance the challenge of trajectory determination and how the wound is interpreted in general. For example, Kieser [48] reported a keyhole entry with the outer cortical layer adjacent to the cortical entry compressed inwards rather than outwards as expected for a keyhole entry wound [49]. The results of high-speed videography may help explain such unusual fragment placements. Observation of impact revealed that kinetic energy imparted to attached fragments results in their dynamic motion and oscillation after the projectile has exited the specimen. Such fragment behaviour in one impact event resulted in the outer cortical layer of one conoid fragment residing below the inner cortical layer of another. When considering fragment position in trajectory determination, it must therefore be kept in mind that their final placement is not necessarily due to a direct interaction with the projectile; rather, it might represent their resting position after dynamic movement has ceased.

The presence and location of bevelling is fundamental to the determination of the entry or exit status of projectile wounds [1, 7], and in this regard, it is significant that some authors have noted its absence in thin areas of bone that lack a

trabecular layer [6, 9, 34]. Whilst the trabecular fracture margin and exit cortical fracture edge will be absent in such bones, the translaminar fracture resulting in bevel formation typically begins as an angulated crack in the outer cortical layer. This angulated crack was restricted to the outer cortical layer in 7 specimens and was also present in a perforated specimen consisting entirely of cortical bone, indicating it forms independently of the trabecular lamina. The possibility therefore arises that cross-sectional analysis may be able to identify the entry or exit status of wounds in thin cortical bone that lacks bevelling. Interestingly, images of angulated entry cortical fracture edges have been captured using multidetector computed tomography (MDCT) [50], suggesting they can be detected in situ during post-mortem analysis.

Whilst the present work focused specifically on sandwich bones, it is important to consider conoidal fracture in a wider skeletal context; at present, it is not clear if this mechanism is responsible for conoidal wound formation during impact in all bone types. For example, Huelke et al. [51, 52] attributed conoidal wound formation in the femoral epiphyses to temporary cavitation of fluid located in the interstices of the trabeculae. Although the formation and dynamic behaviour of bioceramic conoids was captured by the current experimental model, further research is required to confirm that incident kinetic energy drives a process of translaminar fracture and bioceramic conoid formation in human material. Finally, whilst spherical projectiles are ideal for eliminating confounding variables such as deformation on the impact process, future analyses should seek to address the influence of projectile design on perforation mechanisms.

Acknowledgements We are indebted to Alan Peare for running the compressed airgun and high-speed cameras and also for his technical input. We would also like to extend our sincere thanks to Gary Cooper for the design and manufacture of the clamping apparatus.

Compliance with ethical standards

Ethical approval This study was fully approved by the ethics committee of Cranfield University.

Conflict of interest The authors declare that they have no conflict of interest.

References

- Berryman HE, Symes SA (1998) Recognising gunshot and cranial trauma through fracture interpretation. In: Reichs KJ (ed) *Forensic osteology: advances in the identification of human remains*. Charles C Thomas Publishers, Springfield, pp 333–352
- Rhine, Curran (1990) Multiple gunshot wounds to the head: an anthropological review. *J Forensic Sci* 35(3):1236–1245
- Komar DA, Buikstra JE (2008) *Forensic anthropology: contemporary theory and practice*. Oxford University Press Inc., New York
- Kimmerle EH, Baraybar J (2008) *Skeletal trauma: identification of injuries resulting from human rights abuses and armed conflict*. CRC Press, Florida
- Rickman JM, Shackel J (2018) A novel hypothesis for the formation of conoidal wounds in sandwich bones. *Int J Legal Med* 133: 501–519. <https://doi.org/10.1007/s00414-018-1946-x>
- DiMaio VJM (1999) *Gunshot wounds: practical aspects of firearms, ballistics and forensic techniques*. CRC Press, Florida
- Symes SA, L'Abbé EN, Chapman EN, Wolff I, Dirkmaat DC (2012) Interpreting traumatic injuries to bone in medicolegal investigations. In: Dirkmaat DC (ed) *A companion to forensic anthropology*. Wiley- Blackwell Publishing, West Sussex
- Spitz WU (2006) Injuries by gunfire. In: Spitz WU, Spitz DJ, Clark R (eds) *Spitz and Fisher's medicolegal investigation of death: guidelines for the application of pathology to crime investigation*. Charles C Thomas Publishers, Springfield **Available from: Proquest Ebook Central (accessed 8.8.17)**
- Quatrehomme G, İşcan MY (1998) Analysis of bevelling in gunshot entrance wounds. *Forensic Sci Int* 93:45–60
- Rickman JM, Smith MJ (2014) Scanning electron microscope analysis of gunshot defects to bone: an underutilised source of information on ballistic trauma. *J Forensic Sci* 59(6):1473–1486. <https://doi.org/10.1111/1556-4029.12522>
- Olszta MJ, Cheng X, Jee SS, Kumar R, Kim YY, Kaufman MJ, Douglas EP, Gower LB (2007) Bone structure and formation: a new perspective. *Mater Sci Eng R Rep* 58:77–116
- Rho JY, Kuhn-Spearing L, Zioupos P (1997) Mechanical properties and the hierarchical structure of bone. *Med Eng Phys* 20:92–102
- Fratzl P, Weinkamer R (1998) Nature's hierarchical materials. *Prog Mater Sci* 52:1263–1334
- Weiner S, Wagner HD (1998) The material bone: structure-mechanical function relations. *Annu Rev Mater Sci* 28:271–298
- Gray H (1997) *Gray's anatomy*. The promotional reprint company, London
- Hull D (1999) *Fractography: observing, measuring and interpreting fracture surface topography*. Cambridge University Press, Cambridge
- Christensen AM, Passalacqua NV, Bartelink EJ (2014) *Forensic anthropology: current methods and practice*. Academic Press, Oxford
- Peterson BL (1991) External beveling of cranial gunshot entrance wounds. *J Forensic Sci* 36(5):1592–1595
- Kieser JA, Tahere J, Agnew C, Kieser DC, Duncan W, Swain MV, Reeves MT (2011) Morphoscopic analysis of experimentally produced bony wounds from low velocity ballistic impact. *Forensic Sci Med Pathol* 7:322–332. <https://doi.org/10.1007/s12024-011-9240-y>
- Zukas JA (1982) Penetration and perforation of solids. In: Zukas JA, Nicholas T, Swift HF, Greszczuk LB, Curran DR (eds) *Impact dynamics*. John Wiley and Sons, Inc, USA, pp 155–214
- Zaera R, Sánchez-Gálvez V (1998) Analytical modelling of normal and oblique ballistic impact on ceramic/metal lightweight armours. *Int J Impact Engng* 21(3):133–148
- Murphy MS, Gaither C, Goycochea E, Verano JW, Cock G (2010) Violence and weapon-related trauma at Puruchuko-Huaquerones, Peru. *Am J Phys Anthropol* 142:636–649
- Murphy MS, Spatola B, Weathermon R (2014) Allies today, enemies tomorrow: a comparative analysis of perimortem injuries along the biomechanical continuum. In: Martin DL, Anderson CP (eds) *Bioarchaeological and forensic perspectives on violence: how violent death is interpreted from skeletal remains*. Cambridge University Press, Cambridge, pp 261–288
- Bird CE, Fleischman JM (2015) A rare case of an intact bone plug associated with a gunshot exit wound. *J Forensic Sci* 60(4):1074–1077

25. Kieser DC, Riddell R, Kieser JA, Theis J, Swain MV (2013) Bone micro-fracture observations from direct impact of slow velocity projectiles. *J Arch Mil Med* 2(1):e15614. <https://doi.org/10.5812/jamm.15614>
26. Amato JJ, Lawrence BJ, Lawson NS, Norman R (1974) High velocity missile injury. *Am J Surg* 127:454–459
27. Amato JJ, Syracuse D, Seaver PR, Rich N (1989) Bone as a secondary missile: an experimental study in the fragmenting of bone by high velocity missiles. *J Trauma* 29(5):609–612
28. Ragsdale BD, Josselson A (1988) Experimental gunshot fractures. *J Trauma* 28 (No.1 suppl): S109–S115
29. Thali MJ, Kneubuehl BP, Zollinger U, Dirnhoffer R (2002) A study of the morphology of gunshot entrance wounds, in connection with their dynamic creation, utilising the “skin-skull-brain” model. *Forensic Sci Int* 125:190–194
30. Goldsmith W (1960) *Impact: the theory and physical behaviour of colliding solids*. Edward Arnold Publishers, London
31. Wilkins ML (1978) Mechanics of penetration and perforation. *Int J Eng Sci* 16:793–807
32. Currey JD (2002) *Bones: structure and mechanics*. Princeton University Press, New Jersey
33. Dodd MJ (2006) *Terminal ballistics: a text and atlas of gunshot wounds*. CRC Press, Taylor and Francis Group, Florida
34. Loe L (2009) Perimortem trauma. In: Blau S, Ubelaker DH (eds) *Handbook of forensic anthropology and archaeology*. Left Coast Press, California, pp 263–283
35. Abrate S (1998) *Impact on composite structures*. Cambridge University Press, Cambridge
36. Vermeij EJ, Zoon PD, Chang SBCG, Keereweer I, Pieterman R, Gerretsen RRR (2012) Analysis of microtraces in invasive traumas using SEM/EDS. *Forensic Sci Int* 214(1):96–104
37. Spatola BF (2015) Atypical gunshot and blunt force injuries: wounds along the biomechanical continuum. In: Passalacqua NV, Rainwater CW (eds) *Skeletal trauma analysis: case studies in context* pp, pp 7–26
38. Quatrehomme G, Piercecchi-Marti M, Buchet L, Alunni V (2015) Bone bevelling caused by blunt trauma: a case report. *Int J Legal Med* 130(3):771–775. <https://doi.org/10.1007/s00414-015-1293-0>
39. Zeng K, Breder K, Dowcliffe DJ (1992) The Hertzian stress field and formation of cone cracks-I. Theoretical approach. *Acta Metall Mater* 40(10):2595–2600
40. Chen SY, Farris TN, Chandrasekar S (1995) Contact mechanics of Hertzian cone cracking. *Int J Solids Struct* 2(3/4):329–340
41. Lawn BR (1998) Indentation of ceramics with spheres: a century after Hertz. *J Am Ceram Soc* 81(8):1977–1994
42. Berryman HE, Gunther WM (2000) Keyhole defect production in tubular bone. *J Forensic Sci* 45(2):483–487
43. Chaudhri MM (2015) Dynamic fracture of inorganic glasses by hard spherical and conical projectiles. *Philos Trans R Soc Lond A* 373:20140135. <https://doi.org/10.1098/rsta.2014.0135>
44. Piekarski K (1970) Fracture of bone. *J Appl Phys* 41(1):215–223
45. Pope MH, Outwater JO (1972) The fracture characteristics of bone substance. *J Biomech* 5:457–465
46. Pechníková M, Mazzerelli D, Poppa P, Gibelli D, Baggi ES, Cattaneo C (2015) Microscopic pattern of bone fractures as an indicator of blast trauma: a pilot study. *J Forensic Sci* 60(5):1140–1145
47. Ubelaker DH (1996) The remains of Dr Carl Austin Weiss: anthropological analysis. *J Forensic Sci* 41(1):60–79
48. Kieser J (2012) Biomechanics of bone and bony trauma. In: Kieser J, Taylor T, Karr D (eds) *Forensic Biomechanics*. John Wiley & Sons, United Kingdom
49. Dixon DS (1982) Keyhole lesions of the skull and direction of fire. *J Forensic Sci* 23(3):555–566
50. Harcke HT, Levy AD, Getz JM, Robinson SR (2008) MDCT analysis of projectile injury in forensic investigation. *AJR Am J Roentgenol* 190(2):W106–W111
51. Huelke DF, Buege LJ, Harger JH (1967) Bone fractures produced by high velocity impacts. *Am J Anat* 120:123–132
52. Huelke DF, Harger JH, Buege LJ, Dingman HG, Harger DR (1967) Bone fractures produced by high velocity impacts. *J Biomech* 1:97–103

Publisher's note Springer Nature remains neutral with regard to jurisdictional claims in published maps and institutional affiliations.